JOURNAL OF PROPULSION AND POWER
Vol. 25, No. 5, September–October 2009

Infrared Thermography and Pitot Pressure Measurements of a Scramjet Nozzle Flowfield

C. Hirschen* and A. Gülhan†
DLR, German Aerospace Center, 51147 Cologne, Germany

DOI: 10.2514/1.41787

An experimental study on single expansion ramp nozzle flows was carried out at a freestream Mach number of 7 in the hypersonic wind tunnel in Cologne, Germany. The Reynolds number in the tunnel flow was varied to study the performance of the scramjet nozzle at different flight altitudes. The effects of different nozzle pressure ratios were investigated and compared by pitot pressure measurements and schlieren photographs. The temperature distribution on the surface of the single expansion ramp was measured by using infrared thermography. The Stanton number and heat-flux distribution on the surface were determined from measured surface temperature history. Here, it can be seen that the external flow does not influence the temperature distribution. The temperature and Stanton number distribution, however, do depend on the nozzle pressure ratio. A pitot rake was used to measure the pitot pressure distribution in the nozzle wake and characterize the interaction between the nozzle and external flow, as well as the influence of the temperature on the nozzle flow. This showed that the nozzle core flow is independent from the external flow conditions, but the interactions between the two flows are highly dependent. The data obtained by the different measurement techniques gave insight into the properties of single expansion ramp nozzle flows.

Nomenclature

A	=	area, m^2
c	=	speed of light, 3×10^5 km $\cdot$ s^{-1}
c_p	=	specific heat capacity at constant pressure, J kg^{-1} K^{-1}
c_v	=	specific heat capacity at constant volume, J kg^{-1} K^{-1}
h	=	Planck constant, 1.381×10^{-23} J K^{-1}
I	=	momentum, kg m s^{-1}
k	=	Boltzmann constant, 1.381×10^{-23} J K^{-1}
L	=	radiant intensity, W $\cdot$ m^{-3}
M	=	Mach number
n	=	direction normal to the surface
p	=	pressure, N $\cdot$ m^{-2}
$\dot{q}$	=	heat flux, W $\cdot$ m^{-2}
R	=	specific gas constant, m^2 s^{-2} K^{-1}
Re_U	=	unit Reynolds number
St	=	Stanton number
T	=	temperature, K
t	=	time, s
V	=	velocity, m $\cdot$ s^{-1}
x	=	streamwise distance from nozzle entry, mm
y	=	spanwise direction from nozzle centerline, mm
z	=	height above or below flap, mm
α	=	angle of attack, deg
γ	=	heat capacity ratio
ε	=	emissivity
λ	=	wavelength, m
λ	=	heat conductivity coefficient, W $\cdot$ m^{-1} $\cdot$ K^{-1}
ρ	=	density, kg $\cdot$ m^{-3}
σ	=	shock angle, deg
σ_B	=	Stefan–Boltzmann constant, W $\cdot$ m^{-2} $\cdot$ K^{-4}
Π	=	nozzle pressure ratio, $\Pi = p_{0,N}/p_\infty$

Subscripts

amb	=	ambient
cond	=	conductive
conv	=	convective
N	=	nozzle conditions
r	=	radiation
st	=	static
w	=	wall
0	=	total conditions
∞	=	wind-tunnel freestream conditions

I. Introduction

TO SAVE weight and increase the maximum payload of space transportation systems, airbreathing propulsion is an alternative to the existing rocket propulsion systems which carry their oxidant (e.g., liquid oxygen) onboard [1–3]. Aerodynamic stability and generation of sufficient thrust are major problems of a hypersonic vehicle with scramjet propulsion, whereby the nozzle and external base flow interactions play a large role [4]. Although the interaction of the hypersonic nozzle/afterbody flowfield with a cold plume flow has been extensively studied [5–7], there is still a lack of experimental data. It is therefore necessary to study the aerodynamic phenomena which arise from the interaction between the outer base flow and the hot nozzle flow, and to understand their effects on the nozzle performance. This interaction is mainly driven by temperature, viscosity, and heat capacity ratio effects. The infrared (IR) thermography, which provides the temperature and heat-flux distribution on the nozzle surface, contributes an additional data set to existing results [8,9] and improves the physical understanding.

The dynamic interactions between the aerodynamics of the vehicle and the thrust have also been studied numerically [10,11]. Ebrahimi [12] has introduced an efficient design code for scramjet nozzle design. In [13], Ishiguro et al. show the results of a three-dimensional analysis of scramjet nozzle flows which agree well in certain aspects with the experimental results. In [14], the effects on the flow interaction of employing simulant gasses instead of air for the scramjet nozzle flow are presented. Experimental studies investigating the interactions between the external flow and internal nozzle flow have been shown to be very complex and not fully understood as yet [15–17]. In [18], a broad experimental study on the boundary-layer effects in a scramjet nozzle has been carried out. These experimental and numerical studies, however, point to the necessity of further research in this field.

Received 24 October 2008; revision received 26 April 2009; accepted for publication 26 April 2009.

*Ph.D. Student, Wind Tunnel Department of the Institute of Aerodynamics and Flow Technology, Linder Höhe.

†Head of Department, Wind Tunnel Department of the Institute of Aerodynamics and Flow Technology, Linder Höhe. Member AIAA.

As part of a research project that aims to improve the key technologies for the design of a scramjet propulsion unit [19], it is the goal of the present study to investigate the flow of a scramjet nozzle and carry out an experimental study of its performance. Mitani et al. [20] performed an experimental study on the performance of a scramjet nozzle, where they compared the experimental data with the results obtained by an inviscid two-dimensional chemical kinetic code. They showed that lift thrust and main thrust are comparable and very sensitive to the nozzle configuration.

One of the objectives of the present study is to gain information about the nozzle flow of a single expansion ramp nozzle, its interaction with the external flow, as well as the influence of external flow and nozzle total temperature on the nozzle flow. In [21,22], the influence of the heat capacity ratio, nozzle pressure ratio, and freestream Reynolds number on the flow of a three-dimensional single expansion ramp nozzle was already investigated. In [8], the surface pressure distribution was obtained by pressure static measurements (using embedded sensors) and the pressure sensitive paint (PSP) method. This latter method allows the measurement of the pressure distribution on the entire surface of the model and therefore gives more information than the static pressure measurements. In [9], the thrust generated by the nozzle was compared by using the results obtained on the one hand from the embedded sensors and on the other hand from the PSP method. The results of this comparison revealed the advantages of the PSP method when calculating the generated thrust.

In this present work, the influence of external flow and nozzle total temperature on the flow of a two-dimensional single expansion ramp nozzle is studied. Therefore, different measurement techniques are applied and the results are compared with each other. The different measurement techniques enable the visualization of different flow aspects, such as shock positions, shear layer position, and temperature distribution, as well as exhaust plume shape. Shock and shear layer position as well as the shape of the exhaust plume were measured and visualized by means of pitot pressure measurements. These measurements enable the characterization of the interaction between nozzle and external flow. By variation of the nozzle total temperature, the effects on the interaction are studied. It was found that the nozzle total temperature does not influence the shock and shear layer position in the investigated regime. These positions greatly depend on the nozzle pressure ratio. As far as the interactions between nozzle and external flow are concerned, it can be stated that the nozzle core flow is not affected by the external flow conditions.

This model has been designed for a new scramjet project in Germany [19,23] and its performance now has to be investigated. The IR thermography has been applied to obtain temperature and heat-flux distributions over the entire surface of the expansion ramp. Using the one-dimensional heat-flux equation, the heat-flux distribution has been numerically calculated. These experimental investigations showed that temperature and Stanton number distribution are mainly driven by the nozzle pressure ratio and are not dependent on the external flow conditions.

These experiments were performed at a freestream Mach number $M_\infty = 7$ and Reynolds numbers of $Re_U = 4.0 \times 10^6$ and $Re_U = 8.0 \times 10^6$ to simulate different flight altitudes, that is, 30 and 25 km, respectively. According to former experimental studies, the nozzle pressure ratio Π and the freestream Reynolds number Re_U are the main parameters affecting the nozzle flow behavior [21,22,24]. In this present experimental study, the nozzle total temperature is additionally varied to study its influence on the shock and shear layer positions, the exhaust plume shape, the pressure distributions, and the gross thrust.

II. Experimental Methods

A. Wind Tunnel and Test Conditions

The experiments were carried out in the Hypersonic Wind Tunnel Cologne (H2K) of the DLR, German Aerospace Center in Cologne. This facility is a blowdown wind tunnel with test durations of up to 30 s, depending on the flow conditions. The facility is equipped with five contoured nozzles with varying throat diameters and a constant exit diameter of 600 mm, leading to flow Mach numbers of $M_\infty =$ 5.3, 6, 7, 8.7, and 11.2. For these experiments, the $M_\infty = 7$ nozzle was used. Dried air passes from a pressure reservoir with a maximum pressure of 4.5 MPa through electrical heaters with a heating power of 5 MW, thereby heating the air to temperatures of up to 1000 K; this avoids later potential condensation effects in the nozzle expansion. The operational range of the H2K wind tunnel can be seen in Fig. 1a, where the performance map with respect to the Mach number and unit Reynolds number Re_U is depicted, with total pressure p_0 and mass flow rate $\dot{m}$ as parameters. The thick black vertical lines pertain to the available wind-tunnel nozzles. The unit Reynolds number is given by the proper choice of the total pressure p_0 and T_0 of the flow. A schematic sketch of the hypersonic wind-tunnel facility is shown in Fig. 1b.

The wind-tunnel flow conditions for these tests with the nozzle model are summarized in Table 1; the accuracy of measurement is as follows: $\Delta M/M = 0.5\%$, $\Delta T_0/T_0 = 0.75\%$, and $\Delta p_0/p_0 = 0.02\%$.

B. Model and Experimental Setup

Experiments with a single expansion ramp nozzle (SERN) equipped with a generic forebody were carried out (see Fig. 2). The wind-tunnel model was designed in such a modular way that the single parts of the model can be exchanged to provide parametric and geometric variations. The SERN (Fig. 2b) was designed by a tool developed at the wind-tunnel department of the German Aerospace Center to fit the conditions at the end of the combustion chamber of the scramjet vehicle. During these tests, the model and tunnel axes were aligned in parallel.

To provide a uniform flow, a honeycomb followed by a contoured 2-D Laval nozzle (Fig. 2b) was installed inside the settling chamber. The Laval nozzle was necessary to provide supersonic flow and to simulate the Mach number at the combustor exit, which was $M = 2$ for these experiments. The entrance to the SERN has a cross-sectional area of 20 mm height × 80 mm width. More detailed information about the model can be found in [22].

Figure 3 shows a picture of the entire model installed in the wind-tunnel section. It can be seen that the model is held by a strut that is mounted to the side of the model and connected by an adapter to the model to attain a certain separation between the strut and the model. This separation prevents the shock originating from the strut leading edge from perturbing the nozzle flowfield. The strut is mounted to a

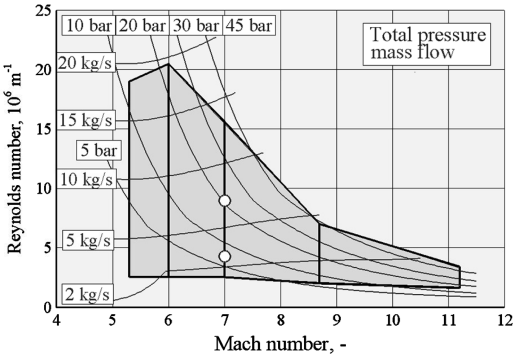

a) Performance map

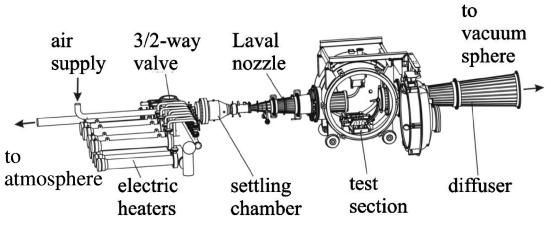

b) Schematic sketch

Fig. 1 Hypersonic wind-tunnel facility H2K.

Table 1 Wind-tunnel flow conditions

Freestream Mach number M_∞	7	7
Freestream pressure p_∞, Pa	260	515
Freestream temperature T_∞, K	60	60
Freestream density ρ_∞, kg/m^3	0.015	0.029
Total temperature T_0, K	650	650
Total pressure p_0, Pa	10×10^5	21×10^5
Unit Reynolds number Re_U	4×10^6	8×10^6

model holder that can be pitched to change the angle of attack and angle of yaw of the model. During a test run, the angle of attack can be varied continuously, whereas only one position for the angle of yaw can be set. The wind-tunnel flow is started as soon as the required pressure in the jet plenum has been achieved. The infrared camera is placed above the model outside the wind tunnel. The camera is mounted in such a way that a perpendicular view onto the SERN is accomplished.

The exhaust gas was supplied to the nozzle plenum by a pipe, which was mounted on the side of the forebody at one end and connected to a tube at the other end. Through this connecting tube, the different gasses, which are stored in external separate reservoirs near the wind tunnel, were injected into the model plenum. To heat the nozzle flow up to temperatures of about 800 K, an additional electrical heater (Fig. 4) of 260 kW power capacity was used. This electrical heater was stored outside the wind tunnel and connected to the wind tunnel through an insulated pipe.

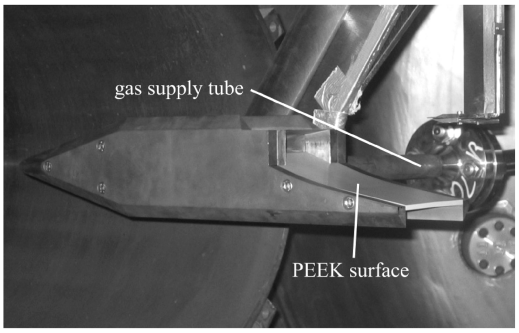

a) Model in wind tunnel

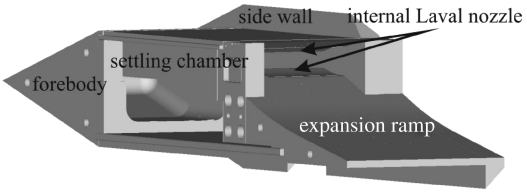

b) 3-D sketch of modular model

Fig. 2 Forebody and nozzle.

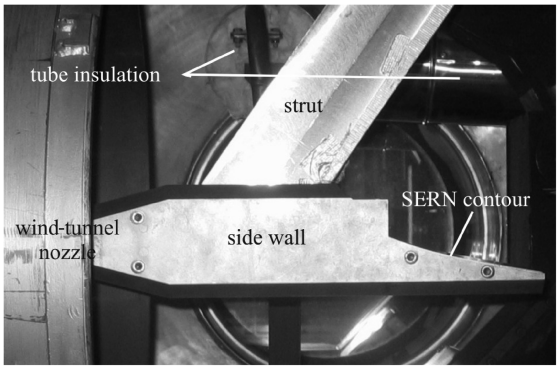

Fig. 3 Side view of the nozzle model connected to a forebody.

C. Measurement Techniques

Because the density and thus the density gradients in H2K are low, a coincident schlieren optical setup is used to visualize the flowfield. With this technique, the light beam traverses the test section twice, which leads to a higher sensitivity. To study unsteady flow phenomena in the nozzle region, a high-speed schlieren camera had been used in a previous experimental study. Based on the results of these experiments, which showed no resolvable unsteady effects, a camera with a higher resolution was used in this experimental study [22].

During the experiments, the jet total pressure $p_{0,N}$ and total temperature $T_{0,N}$ are measured with a pitot tube and a thermocouple in the settling chamber downstream of the honeycomb and upstream of the internal Laval nozzle. The static pressures on the SERN are measured with a Pressure Systems, Inc. (PSI) module with the range of 15 psi (∼105 kPa).

1. *Pitot Pressure Measurements*

To obtain a pressure distribution of the flowfield, pitot pressure measurements were carried out. The pitot rake had 26 pitot probes placed 6 mm apart, leading to a total pitot rake span of 150 mm. To measure the pitot pressure distribution in the entire flowfield, the pitot rake is displaced in axial x and vertical z directions. Figure 5 shows the displacement unit; the coordinate system used is also shown. The pitot rake is mounted to a rod which is moved in a vertical direction by a linear motor, and a potentiometer is used to measure its position. The entire unit of drive and control unit, potentiometer, rod, and pitot rake can be moved in the x (flow) direction. The measurement of the pitot pressure at different z and x positions enables a mapping of the flow over and downstream of the nozzle. The achieved spatial resolution of this process depends on the adopted step sizes in the z and x directions: here, $\Delta z = 2$ mm and $\Delta x = 50$ mm were used. Hence, for each x position, a grid of points in the y–z plane is measured; with $\Delta y = 6$ mm and $\Delta z = 2$ mm as the grid spacing, the representation as a continuous flowfield can be obtained by interpolating between the discrete points.

The pitot tubes are also connected to a PSI module with the same operating range of 15 psi (∼105 kPa), which records and then digitizes the pressure values in a scanner interface, at which point they are sent to a computer. For more details on how the pitot measurements are carried out and how the flow properties are ascertained, see [8].

2. *Infrared Thermography*

The IR thermography is used to obtain the temperature distribution on the surface of the SERN. These data are then used to numerically calculate the heat flux into and the heat loads onto the surface of the SERN. The advantages of the IR thermography are that the temper-

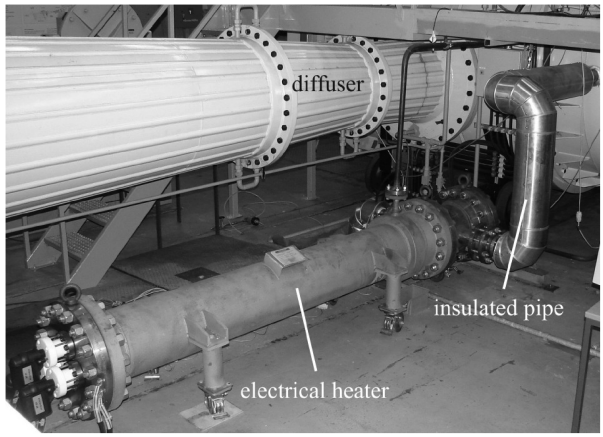

Fig. 4 Electrical heater outside the wind tunnel.

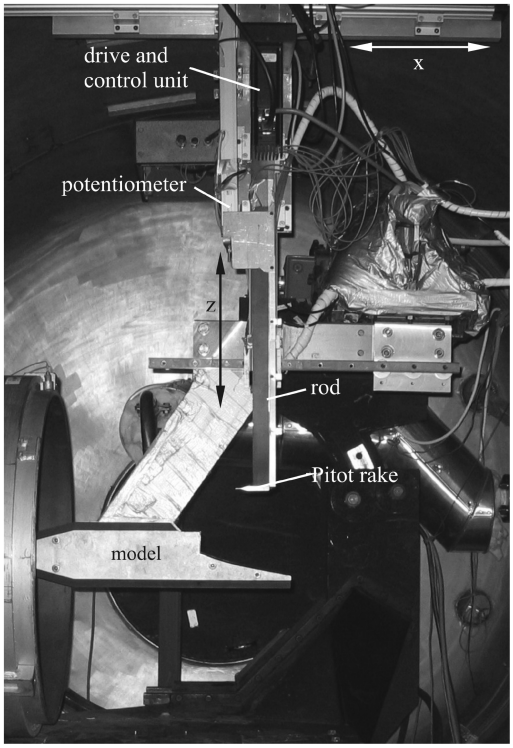

Fig. 5 Pitot rake displacement unit.

ature distribution can be measured nonintrusively and on the entire surface, whereas thermocouples only measure the local temperature and also influence the surface characteristics [25]. The heat-flux distribution is obtained by applying the one-dimensional unsteady heat equation normal to the surface [26], Eqs. (3) and (4), and taking the temperature distribution as boundary conditions into account. To measure the temperature distribution over the entire surface of the SERN, an infrared camera system is used. This infrared camera receives the radiant intensity L, which is emitted from the surface and is used to calculate the wall temperature by applying Planck's radiation law. With the known wavelength λ and emissivity ε, the wall temperature can be obtained by Eq. (3):

$$T_w = \frac{c_2}{\lambda}\frac{1}{\ell_n[1+(\varepsilon c_1)/(L\lambda^5)]} \quad \text{with} \quad c_1 = 2\pi hc^2 \quad \text{and} \quad c_2 = \frac{hc}{k} \tag{3}$$

In this equation, h represents the Planck constant, c the speed of light, and k the Boltzmann constant. The temperature distribution is then processed and stored in a three-dimensional data array $[x, y, t]$. With Eqs. (4) and (5), the temperature gradient can be calculated and thus the heat flux onto the surface $\dot{q}_{\text{cond}}$, which is calculated using Eq. (6):

$$\rho(T)c_V(T)\frac{\partial T}{\partial t} = \frac{\partial}{\partial n}\left(\lambda(T)\frac{\partial T}{\partial n}\right) \tag{4}$$

$$\rho(T)c_V(T)\frac{\partial T}{\partial t} = \frac{\partial\lambda(T)}{\partial n}\frac{\partial T}{\partial n} + \lambda(T)\frac{\partial^2 T}{\partial n^2}$$
$$\rightarrow \rho(T)c_V(T)\frac{\partial T}{\partial t} = \frac{\partial\lambda(T)}{\partial T}\left(\frac{\partial T}{\partial n}\right)^2 + \lambda(T)\frac{\partial^2 T}{\partial n^2} \tag{5}$$

$$\dot{q}_{\text{cond}} = -\lambda_W\frac{\partial T}{\partial n} \tag{6}$$

The convective heat from the fluid onto the surface of the model $\dot{q}_{\text{conv}}$ equals the sum of the radiated and conducted heat flux [Eq. (7)], whereas the radiated heat flux $\dot{q}_r$ is calculated according to the Stefan–Boltzmann equation [Eq. (8)] and the conducted heat according to the one-dimensional heat equation [Eqs. (4–6)]. In Fig. 6, the relation between the different heat fluxes is depicted:

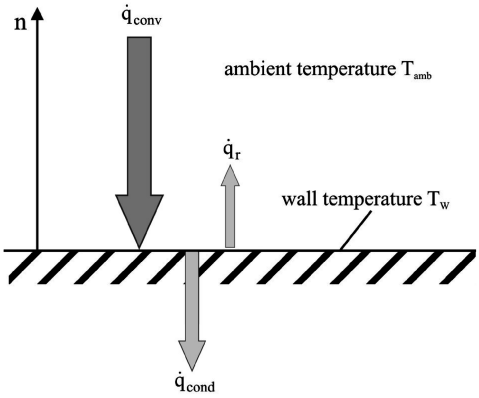

Fig. 6 One-dimensional relation between the heat fluxes on the model surface.

$$\dot{q}_{\text{conv}} = \dot{q}_{\text{cond}} + \dot{q}_r \tag{7}$$

$$\dot{q}_r = \sigma_B\varepsilon(T_W^4 - T_{\text{amb}}^4) \quad \text{with} \quad \sigma_B = 5.6686\times10^{8}\ \text{W}\cdot\text{m}^{-2}\cdot\text{K}^{-4} \tag{8}$$

For the experiments, a SERN manufactured out of PEEK (polyetheretherketone) was used. This is a material with low heat conductivity as well as well-known material parameters such as the emissivity, heat conduction, heat capacity, and density in the temperature range of $300 < T < 600$ K. The material parameters of PEEK were measured by the DLR Institute for Materials Research in Cologne. The emissivity for PEEK was measured as 0.95. For the density, heat capacity, and heat conduction, Eqs. (9–11) are to be used:

$$\rho_{\text{PEEK}} = 1.29\times10^{3}\ \text{kg}\cdot\text{m}^{-3} \tag{9}$$

$$c_{V_{\text{PEEK}}} = 6.1\ \text{J kg}^{-1}\text{K}^{-1} + 3.5\ \text{J kg}^{-1}\text{K}^{-2}\,T \tag{10}$$

$$\lambda_{\text{PEEK}} = -2.98\times10^{-1}\ \frac{\text{W}}{\text{m K}} + 4.14\times10^{-3}\ \frac{\text{W}}{\text{m K}^2}T - 1.01\times10^{-5}\ \frac{\text{W}}{\text{m K}^3}T^2 + 8.16\times10^{-9}\ \frac{\text{W}}{\text{m K}^4}T^3 \tag{11}$$

A low heat conductivity is necessary to guarantee that the semi-infinite wall assumption is valid and the heat flux in the plane of the surface can be neglected compared to heat flux perpendicular to the surface plane. It is mandatory to know the emissivity of the used material to obtain the correct temperature and heat-flux distribution by the IR thermography. In [27], it is shown that the calculated heat-flux values match the analytical results. The temperature and heat-flux distribution is important to estimate the heat loads on the SERN of a scramjet engine.

III. Experimental Results and Discussion

A. Influence of Nozzle Total Temperature

The nozzle total temperature is varied to study its influence on the pressure distribution and the interaction between the nozzle and external flow. Figure 7 shows the influence of the nozzle total temperature on the static pressure distribution along the centerline of the expansion ramp. The nozzle total temperature $T_{0,N}$ varies between 295 and 758 K, leading to significant differences in the velocity and density of the flow.

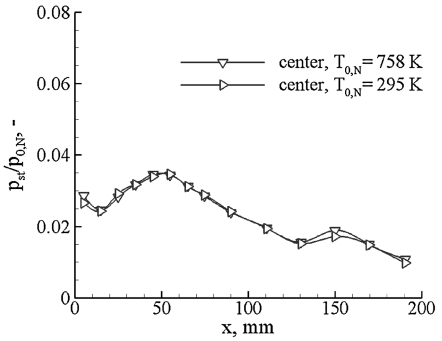

Fig. 7 Influence of the nozzle total temperature on the static pressure distribution along the centerline at $Re_U = 4 \times 10^6$ and $\Pi = 500$.

As can be seen, the differences in the pressure distribution for a nozzle pressure ratio of $\Pi = 500$ and a temperature difference of about $\Delta T = 460$ K are very small and negligible. In this case, the gross thrust is not influenced by the nozzle total temperature in the investigated temperature regime, because the effects of a higher velocity and a lower density cancel each other. This can be seen in Eq. (12) for the momentum change:

$$\frac{\mathrm{d}I}{\mathrm{d}t} = \rho V^2 A = \frac{p}{RT}(M\sqrt{\gamma RT})^2 A = pM^2\gamma A \tag{12}$$

This equation shows that the heat capacity ratio has an influence on the momentum. The heat capacity ratio of air starts to change at a static temperature of $T > 300$ K. Such a high static temperature and thereby a change of the heat capacity ratio in the Mach number regime ($M > 2$) are only obtained at a nozzle total temperature above 1000 K. The nozzle total temperature has to be increased significantly (above 2500 K) to simulate the proper heat capacity ratio of a real combustion gas. This higher temperature would lead to a dissociation of air which inhibits the assumption of a thermally perfect gas [28]. For this reason, this high temperature is not applicable in wind-tunnel tests. The static pressure distribution therefore mainly depends on the nozzle pressure ratio and the nozzle geometry in the investigated temperature regime. Concerning the pressure distribution at the beginning of the expansion ramp ($x < 50$ mm), the somewhat abnormal distribution catches attention: It is expected that the slope of the distribution curve is negative in this region, because the pressure is supposed to decline due to the expansion. The pressure, however, climbs again between the second and sixth pressure tab after the pressure decline between the first two pressure tabs. The reason for this is supposedly the internal Laval nozzle. If the flow conditions do not exactly match the design conditions, expansion and compression waves generated by the Laval nozzle are reflected at the walls and cause the pressure increase [29]. A second pressure increase is located at the streamwise position $x = 150$ mm where the expansion waves generated at the corners of the side walls interact and lead to the pressure increase (Fig. 8).

The schlieren photographs (Figs. 9a and 9b) show how the nozzle total temperature affects the interaction between the nozzle and the external flow. Previous experimental investigations [30] described the influence of the nozzle total temperature on the pressure distribution and the shape of the exhaust plume. In the investigated regime in this present work, these observations cannot be confirmed. There is no effect on the pressure distribution and the schlieren photographs do not show any influence on the shape of the exhaust plume. For the same size of the exhaust plume, the deflection of the external flow is identical, hence the angle of the external shock σ also equals. Under identical conditions in the external flow (M and Re_U), the external shock causes the same pressure loss due to this shock. The base drag depending on this pressure loss does not change in this case and is independent from the nozzle total temperature in this regime. The gross thrust is also independent from the nozzle total temperature because the pressure distributions are almost identical for the different nozzle total temperatures and the momentum change mainly depends on the pressure (at a temperature range between 300 and 1000 K). Therefore, the influence of the nozzle on the gross thrust and the interactions between the nozzle and external flow, thus on the base drag, are very small and negligible, respectively, in the investigated regime.

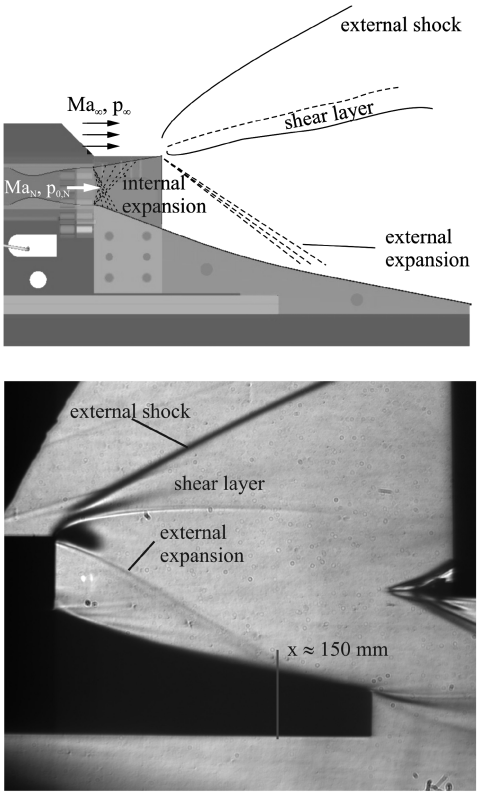

Fig. 8 Flow topology and characteristics of nozzle flow originating at the nozzle entry: top, schematic; bottom, schlieren photograph.

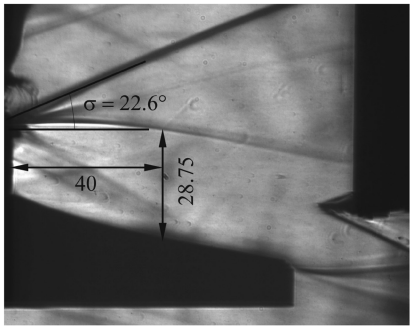

a) $T_{0,N}$ = 300 K

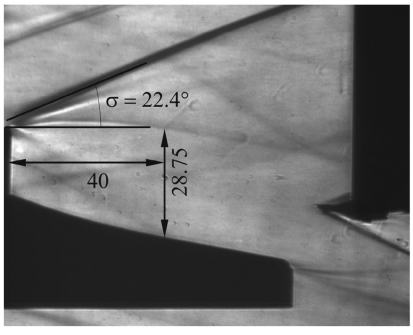

b) $T_{0,N}$ = 800 K

Fig. 9 Influence of the nozzle total temperature on the interaction between the nozzle and external flow at $Re_U = 8 \times 10^6$ and $\Pi = 250$.

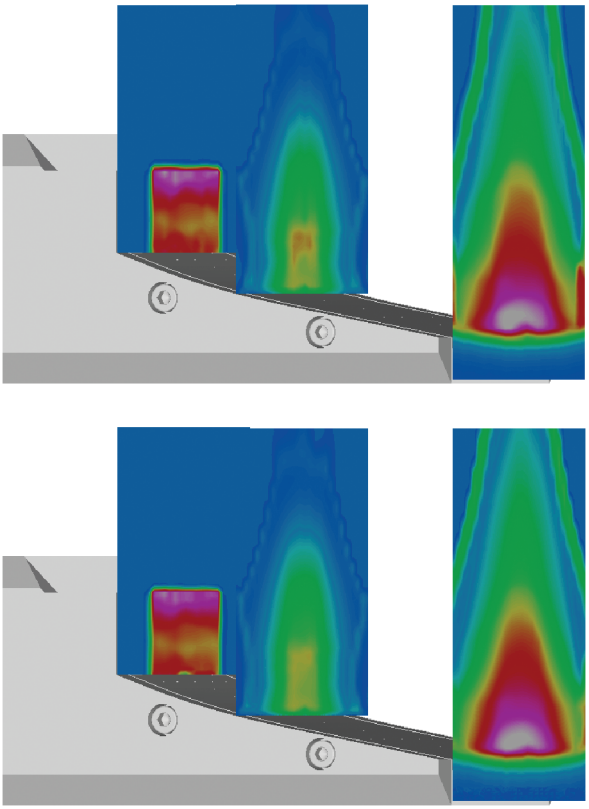

Fig. 10 Influence of the nozzle total temperature on the nozzle flowfield without external flow at $\Pi = 500$ in three different planes: top, $T_{0,N} = 300$ K; bottom, $T_{0,N} = 750$ K.

In Fig. 10, the influence of the nozzle total temperature on the pitot pressure distribution in the nozzle flowfield is investigated. Three different planes in the streamwise direction are compared at two different nozzle total temperatures ($T_{0,N} = 300$ K and $T_{0,N} = 750$ K) without external flow. In this case, the nozzle flow is not influenced by the external flow and vice versa so that the following flowfield is established (Fig. 10). In this depiction, the legend for the pressure is neglected, because the qualitative comparison is more important. The scale is equal for the first two planes ($x = 40$ mm and $x = 100$ mm, $0 < p_{\text{pitot}}/p_{0,N} < 0.5$), but different in the third plane ($x = 210$ mm, $0 < p_{\text{pitot}}/p_{0,N} < 0.1$). In the third plane, the pitot pressure is much smaller and therefore a finer scale is needed to reveal the flow topology. The measured pitot pressure decreases in the streamwise direction due to the expansion of the flow and the velocity increase. The higher the flow velocity is, the higher is the total pressure loss over the normal shock caused by every single pitot tube. For this reason, a low pitot pressure indicates a high flow velocity in the region of the nozzle flow, where the nozzle total pressure is assumed to be constant. Outside the shock, this assumption is not valid anymore.

From the three planes, it can be observed that the nozzle flow expands after leaving the internal nozzle area. In the first plane ($x = 40$ mm), the nozzle flow has a shape of a square. In the streamwise direction, the nozzle flow then proceeds and expands in y and z directions, so that a flow topology typical for such a nozzle flow develops in the second plane ($x = 100$ mm). The decrease of the pitot pressure in y and z directions is clearly seen due to the acceleration in these directions. Therefore, the flow topology converges from the square shaped to a more triangular shaped one. But the temperature does not affect this shape, neither the position of the shear layer, nor the shocks in the investigated temperature regime.

Figures 11 and 12 show the influence of the nozzle total temperature on the flowfield in the wake of the nozzle at a nozzle pressure ratio of $\Pi = 500$ with and without external flow at the downstream position $x = 210$ mm. The flowfield in the wake is depicted by the pitot pressure measurements in the y–z plane in such a way that the flow topology becomes visible. The results of the pitot pressure measurements do not show any influence of the nozzle total temperature in the researched regime. No remarkable differences can be seen between the highest ($T_{0,N} = 798$ K) and the lowest ($T_{0,N} =$ 307 K) nozzle total temperature. Small deviations of the position of the external shock are caused by the fact that the nozzle pressure ratio is not exactly the same. In the case with external flow (Fig. 11), the nozzle flow is highly affected by the external flow, leading to a triangular shape of the flow only in the core nozzle flow, whereas this triangular shape cannot be observed in the external flow. In the upper region of each plane, the external flow has the main influence and, in the upper right corner, the perturbations generated by the strut of the model can be seen. From the leading edge of the strut, an oblique shock wave emanates and propagates into the measurement plane, leading to an asymmetrical flowfield in the upper region. The lower region is not affected by this shock and remains symmetrical, as can clearly be seen. At a lower nozzle pressure ratio $\Pi = 250$, the nozzle flow is more strongly affected by the external than at higher nozzle pressure ratios, for the nozzle flow at lower nozzle pressure ratios deflects the external flow less than at higher nozzle pressure ratios. Besides these small differences between the three measurement planes, the impact of the nozzle total temperature on the flowfield in the wake of the nozzle is very little in the investigated regime.

The results of the pitot pressure measurements at a nozzle pressure ratio $\Pi = 500$ without external flow are depicted in Fig. 12. In contrast to the results shown in Fig. 11, the perturbations originating from the strut do not exist. For this reason, the measurement plane is completely symmetrical, proving the nozzle flow to be symmetrical

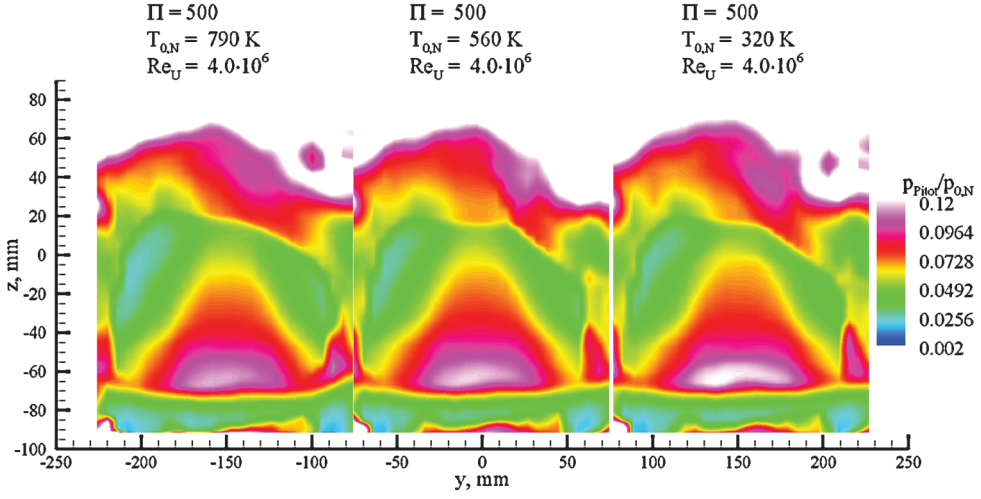

Fig. 11 Influence of the nozzle total temperature on the flowfield in the wake of the nozzle at $Re_U = 4 \times 10^6$, $\Pi = 500$, and the streamwise position $x = 210$ mm.

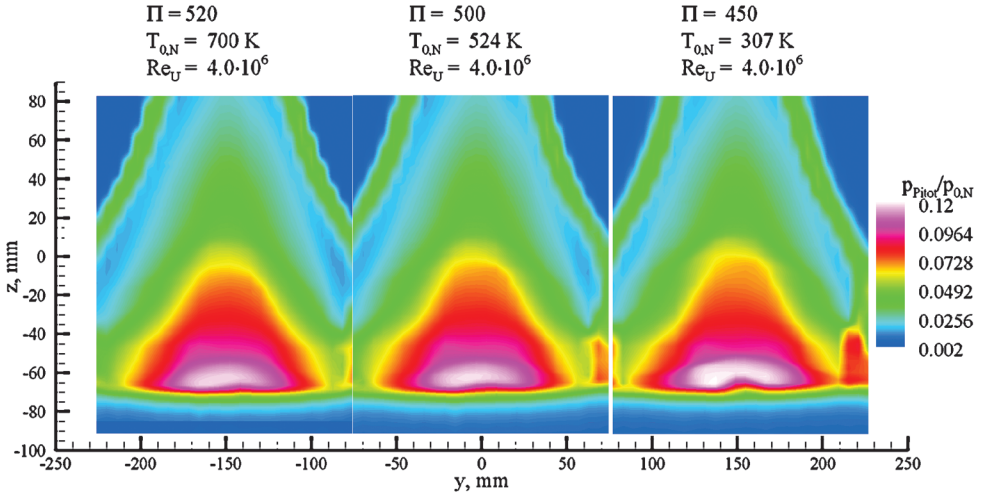

Fig. 12 Influence of the nozzle total temperature on the flowfield in the wake of the nozzle without external flow at $\Pi = 500$ and the streamwise position $x = 210$ mm.

as well. Small deviations of the position of the shear layer and the external shock are in this case also caused by the slightly different nozzle pressure ratio. The experimental investigations show that the nozzle pressure ratio mainly affects the position of shear layers and shocks. The size and the position of the high-pressure region in the core of the nozzle flow are almost identical and thereby independent from the nozzle total temperature in the investigated regime. The side-by-side comparison of the three measurement planes reveals that the position of the shear layer and the shocks at the end of the expansion ramp (in this view, in the lower part at around $z = -90$ mm) is nearly equal at all three nozzle total temperatures.

B. Temperature and Stanton Number Distribution

With the IR thermography, the temperature and Stanton number distribution of hot nozzle flows is measured on the nozzle surface. For the evaluation of the IR thermography, the material of the nozzle must have a low heat conductivity, and the material parameters have to be known. Therefore, for the present experimental study, the nozzle was manufactured out of PEEK, which allows a maximal nozzle total temperature of about 580 K. Figure 13 shows the temperature and Stanton number distribution at $\Pi = 500$ and $Re_U = 8 \times 10^6$. The IR thermography helps to estimate the influence of the nozzle pressure ratio on the temperature and Stanton number distribution. The Stanton number represents the dimensionless heat flux and is calculated with the following Eq. (13):

$$St = \frac{\dot{q}_c}{c_p \rho_{\infty,N} V_{\infty,N} (T_{0,N} - T_w)} \tag{13}$$

In the equation, c_p, $\rho_{\infty,N}$, $V_{\infty,N}$, and $T_{0,N}$ are parameters of the nozzle flow measured and calculated at the nozzle entrance. The static temperature on the surface of the expansion ramp is not constant along the entire surface, but dependent on the position. Because of the side expansion, the nozzle accelerates at the side corners leading to a heterogeneous Mach number distribution on the expansion ramp. This Mach number distribution leads to the specific temperature distribution which causes the present Stanton number distribution. The nozzle flow expands more strongly along the freestream rim of the nozzle plume, leading to a higher Mach number in this region than in the core of the nozzle flow. For a constant nozzle total temperature, the static temperature decreases according to the Mach number distribution.

Furthermore, the static pressure follows the Mach number distribution in such a way that the static pressure decreases where the Mach number increases. A lower static pressure causes a lower Reynolds number and thereby a thicker boundary layer. Because of the thicker boundary layer, the temperature gradient from the flow to the wall decreases, leading to a lower temperature and heat flux onto the surface in the regions of higher Mach number. Therefore, the Stanton number is also lower where temperature and heat flux are lower. Figure 14 shows that the temperature and pressure distribution on the expansion ramp qualitatively agree very well. The temperature distribution thereby represents the flow topology caused by the three-dimensional expansion. It directly influences the heat-flux distribution, because high-temperature differences also cause high heat fluxes and vice versa. The Stanton number distribution in Fig. 13, being qualitatively identical to the temperature distribution, confirms this observation.

The knowledge of the temperature and Stanton number distribution supports the design of a suitable cooling system of the nozzle surface. Depending on the heat loads, a suitable cooling system is designed in such a way that it is neither over- nor underdimensioned. Overdimensioning increases the total mass of the propulsion engine and decreases the thrust; this latter effect should not be neglected.

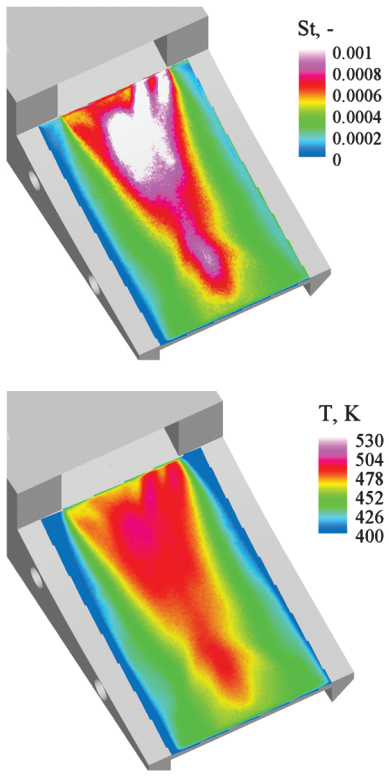

Fig. 13 Stanton number (top) and temperature (bottom) distribution at $\Pi = 500$ and $Re_U = 8 \times 10^6$.

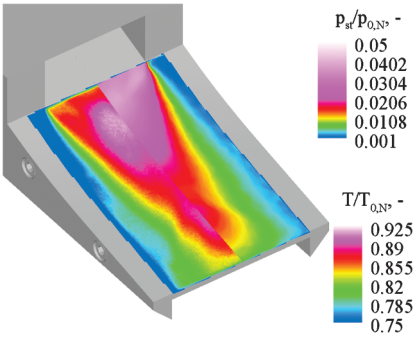

Fig. 14 Comparison of the temperature (left side) and pressure (right side) distribution along the expansion ramp at $\Pi = 500$ and $Re_U = 8 \times 10^6$.

Underdimensioning causes material and also engine failure, which has to be avoided. A sophisticated cooling system does not have to reduce the heat loads along the entire expansion ramp, but only at the locations where the heat loads extend the maximal tolerable loads.

C. Nozzle Pressure Ratio

Figure 15 compares the influence of the nozzle pressure ratio on the static pressure distribution along the cowl and the centerline of the expansion ramp. The static pressure is normalized by the nozzle total pressure $p_{0,N}$. The nozzle pressure ratio affects this relation only slightly in the investigated regime. Therefore, its influence is negligible in this regime, that is, the qualitative distribution of the static pressure does not depend on the pressure ratio. It is remarkable that, after the strong pressure decrease at the beginning of the expansion ramp due to the expansion, the pressure increases again. The reason for this is the expansion and compression waves that emanate from the Laval nozzle inside the model and reflect at the walls. Because of boundary-layer effects, it is possible that the flow conditions do not match the conditions for the originally designed Laval nozzle generating the expansion and compression waves; these waves cause perturbations inside the nozzle flow that lead to the pressure increase. This effect is also described in [29]. Further downstream at $x =$ 150 mm, the static pressure increases again slightly. This position is the location where the expansion waves originating from the side corners intersect. In the intersection point, the expansion waves are reflected as compression waves causing the pressure to increase. Because the nozzle flow accelerates further, the pressure decreases further downstream of this point. On the cowl, a similar pressure distribution is observed: the pressure declines due to the expansion and climbs due to the expansion and compression waves. The fact that the pressure curves on the cowl are so close to each other shows that the nozzle pressure ratio does not influence the pressure distribution on the cowl either in the investigated regime.

1. *Pitot Pressure Results*

Pitot pressure measurements image the spatial flowfield in the wake of the nozzle. The following Figs. 16a–16f show the flowfield

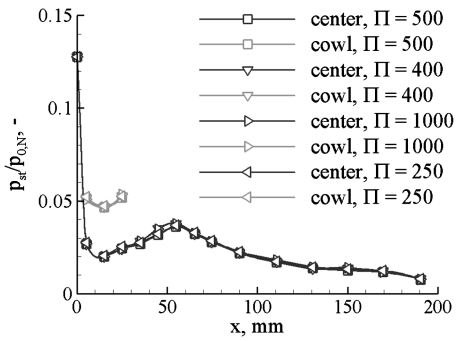

Fig. 15 Influence of the nozzle pressure ratio on the static pressure distribution at $Re_U = 4 \times 10^6$.

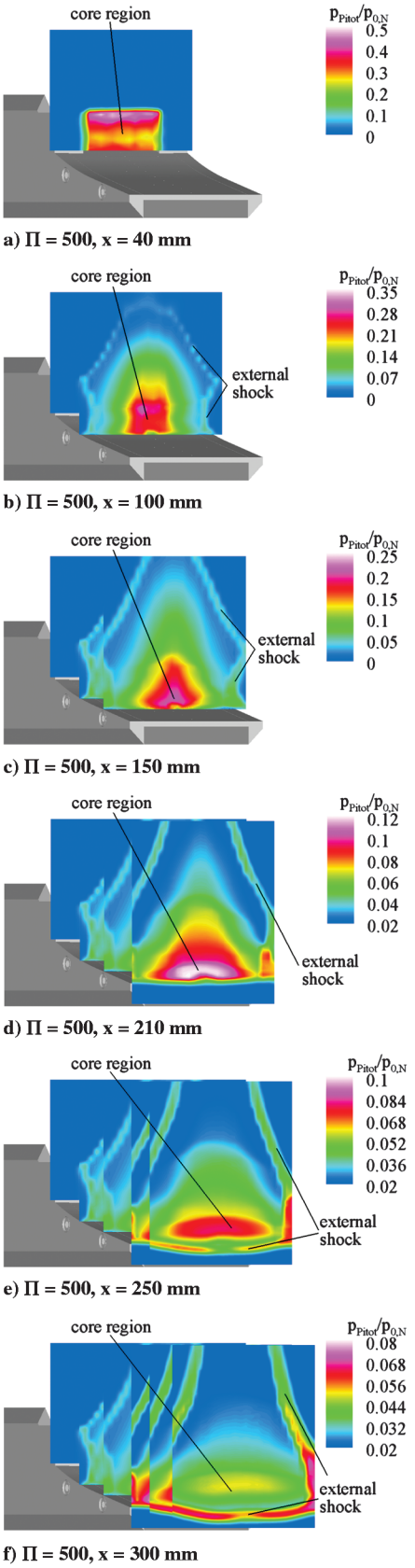

Fig. 16 Pitot pressure measurements in six different measurement planes inside the nozzle flow without external flow at $\Pi = 500$.

and the topology of the nozzle flow in six different measurement planes downstream of the nozzle entry without external flow. The core region of the nozzle flow is of rectangular shape and symmetrical in the measurement plane $x = 40$ mm shortly after leaving the closed (by side walls) nozzle region. The nozzle flow is established

over the entire width of 80 mm. Further downstream at $x = 100$ mm, the effects of the three-dimensional expansion in y and z directions are noticed. The rectangular region shrinks and the nozzle flow expands and accelerates in any possible direction. An external shock emerges to match the ambient static pressure. This external shock has the shape of a bow.

In the next measurement plane $x = 150$ mm, the core region becomes triangular due to the expansion. The bow shape of the external shock also becomes triangular. This shape becomes even more significant 60 mm further downstream in the measurement plane $x = 210$ mm, so that the nozzle flow is limited by a triangle in the upper region. The shape of the core region also looks like a triangle in this measurement plane. The distance between the external shock on the right and the left side increases from the first to this measurement plane, characterizing the increase of the exhaust plume.

It can be seen that the triangular shape of the core region starts to vanish in the measurement plane $x = 250$ mm and become a more elliptical shape. This tendency is enhanced continuously until the last measurement plane $x = 300$ mm. In the last three planes, the shear layer and the external shock can be noticed in the lower part of the nozzle flow originating at the end of the expansion ramp (x= 210 mm). The depiction of the different measurement planes gives a detailed image of the origin and the development of the nozzle flow with its characteristic flow topology.

The pitot rake is placed at the position $x = 210$ mm, that is, 10 mm behind the nozzle end, to study the influence of the nozzle pressure ratio on the nozzle flow. Figures 17a–17c show the results of the pitot pressure measurements without external flow and at three different nozzle pressure ratios: 500, 250, and 190. The nozzle flow in the wake of the nozzle strongly depends on the nozzle pressure ratio. This mainly regards the position of the external shock as well as the size of the exhaust plume. The core region of the nozzle flow along the expansion ramp mostly remains independent, as the three pictures show. The reason for that is that a higher nozzle pressure ratio only displaces the freestream rim of the nozzle plume, whereas the flow along the solid expansion ramp cannot be displaced.

With decreasing nozzle pressure ratio, the triangle shrinks more and more in the upper part of each measurement plane. Because the expansion is weaker due to the lower nozzle pressure ratio, the Mach numbers and flow velocities are also lower. A sign for that is the higher pitot pressure in the region of the external flow. As mentioned before, a higher pitot pressure comes along with a lower Mach number at a constant nozzle total pressure. The loss over the normal shock in front of the pitot tube increases with the Mach number, leading to a lower pitot pressure at a higher Mach number. The nozzle pressure ratio affects not only the size of the exhaust plume and position of the external shock, but also the velocity distribution due to the strength of the expansion. The stronger expansion in the case of a higher nozzle pressure ratio enlarges the exhaust plume in y and z directions compared to smaller nozzle pressure ratios. The size of the exhaust plume influences the base drag of the nozzle and the entire propulsion unit: With an external flow, as in the real flight, the displacement of the external flow is smaller at lower nozzle pressure ratios and so is the drag due to the shocks caused by the displacement.

Along the expansion ramp, the flowfield does not change comparing the planes for the three nozzle pressure ratios. The region of higher pressure between $y = -40$ mm and $y = 40$ mm, as well as between $z = -70$ mm and $z = -40$ mm (core region), is very similar in all three cases. The nozzle flow along the expansion ramp seems to be independent from the nozzle pressure ratio, proving the observations from PSP measurements [9]. The velocity in the core region depends on its position in the flow direction and is independent from the nozzle pressure ratio. But the nozzle pressure ratio highly affects the strength of the nozzle flow expansion.

The comparison between pitot pressure measurements and schlieren photographs shows that the position of the shear layer and shock is detected correctly. In Fig. 18a, four measurement planes are superposed on the schlieren photograph. The positions of shear layer, internal, and external shock agree very well. The position of the external shock in the schlieren photograph is marked by the thick black line. This line intersects the pitot measurement plane exactly at

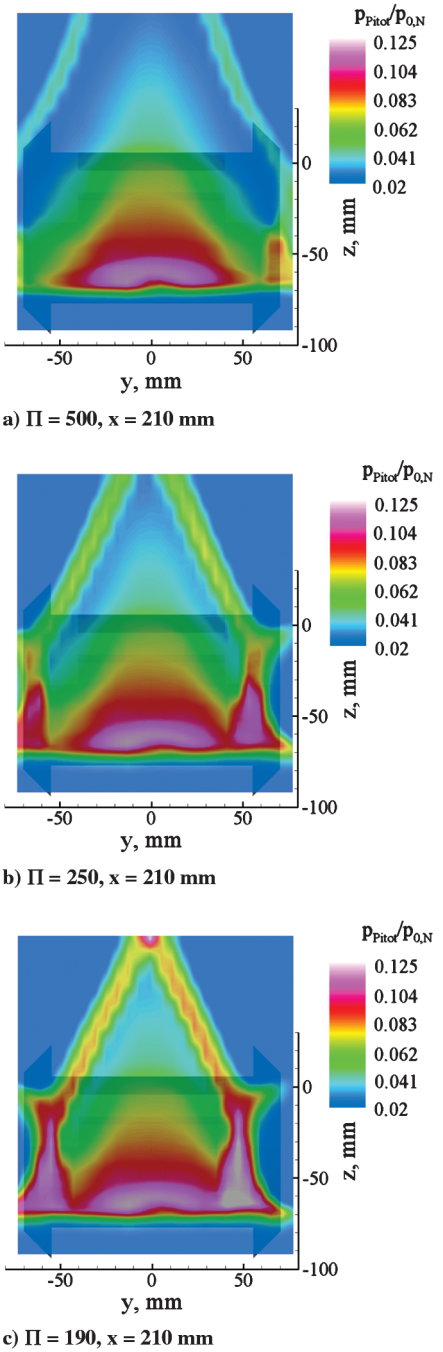

Fig. 17 Pitot pressure measurements at different Π ($x = 210$ mm is the same in each figure).

the position where a pressure increase can be found in the measurement plane. The internal shock is marked by a dark gray crooked line in the schlieren photograph (Fig. 18b) and also intersects the measurement plane where a pressure increase can be found (Fig. 18a). This comparison gives trust that the remaining three-dimensional flow topology and its gradients are measured and detected correctly by the pitot pressure measurements. The advantage of the pitot pressure measurements compared to the schlieren photographs is that the schlieren photographs only provide two-dimensional information, whereas the pitot pressure measurements supply three-dimensional information in different measurement planes.

Figure 19 provides a detailed image of the pitot measurement plane $x = 150$ mm; in the left picture, the pitot pressure at $y = 0$ mm is superposed on the schlieren photograph. It can be seen that the positions where the pitot pressure curve changes its slope, the internal and external shock is to be found. In the right picture, however, the pitot pressure of the entire plane is depicted to show the

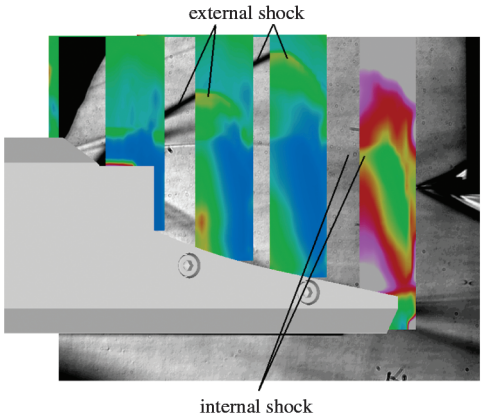

a) Pitot pressure measurement and schlieren photograph

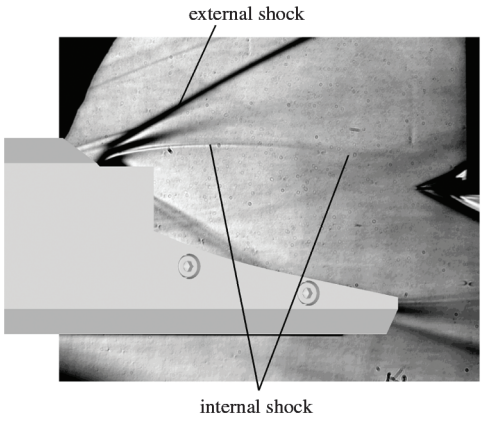

b) Schlieren photograph

Fig. 18 Comparison of the pitot pressure measurements with the schlieren photograph in different measurement planes at $\Pi = 500$.

good agreement in this view. A strong pressure increase is found at $z = 50$ mm, because the total pressure of the external flow is much greater than the one of the nozzle flow (8 times). Shortly underneath the position $z = 50$ mm, the pitot pressure decreases due to the shock and the total pressure loss. Over the shear layer, the static pressure of the external and the nozzle flow match each other. In this region of the nozzle flow, the total pressure continuously decreases from its maximal value near the expansion ramp to the position $z = 20$ mm. The reason for this is the expansion of the nozzle flow only in the direction toward the freestream rim of the exhaust plume. The acceleration related to this expansion leads to the pressure decrease. At the position $z = 20$ mm, the pressure increases again due to the internal shock. The horizontal line between the two pictures points out the good agreement.

In the next measurement plane, $x = 210$ mm, directly behind the end of the expansion ramp, the comparison between the pitot pressure measurements and the schlieren photograph looks as follows (Fig. 20): The external shock is not detected by the pitot pressure measurements, because the angle of the shock is too great, so that the shock is outside of this measurement plane. The internal shock, however, moved to the position $z = 12$ mm due to the bow shape of the internal shock. From this point on, the exhaust plume shrinks again. At the position $z = -60$ mm (very close to the expansion ramp) the location with the greatest pitot pressure and thereby with the lowest Mach number is found. The external shock at the end of the expansion ramp is detected in this measurement plane, because the pitot rake is placed 10 mm behind the expansion ramp. External and internal shock are so close to each other that they cannot be distinguished properly and appear as one single gradient in the pitot pressure curve in the left picture. In the right picture, the three-dimensional topology of the nozzle flow is noticeable, which is caused by the expansion in the y and z directions.

2. *Infrared Thermography Results*

In Fig. 21, the affects on the Stanton distribution are depicted when varying the nozzle pressure ratio. If the nozzle pressure ratio is increased, the temperature and the heat flux on the surface of the expansion ramp also increase. One reason for this observation is the increased mass flux due to the higher nozzle pressure ratio. For the same nozzle total temperature, the heat quantity of the flow that is transferred from the flow to the surface increases with the mass flux. The more heat that is transferred from the flow to the surface, the higher are the temperature on the surface and the heat flux onto the surface. Furthermore, the local Reynolds number increases with increasing pressure, leading to a thinner boundary layer. Therefore, the temperature gradient from the nozzle flow to the wall enlarges. The heat flux is proportional to the temperature gradient so that the heat flux increases with increasing nozzle pressure ratio. It has to be taken into account that a higher nozzle pressure ratio leads to a higher gross thrust, but it also needs a higher cooling capacity to avoid structural failure. This causes a higher total mass of the engine and decreases its performance.

It can be stated that the nozzle pressure ratio hardly influences the qualitative temperature and Stanton number distribution. Clearly seen are the hot spots centered at the beginning of the expansion ramp; they agree well with the spots of the greatest heat fluxes. In the outer region, temperature and Stanton number decline. The reason for this distribution is the Mach number distribution due to the three-dimensional expansion. The expansion leads to a certain Mach number distribution along the expansion ramp in the x, y, and z directions, which is not constant. The Mach number distribution then causes the present temperature and Stanton number distribution: high temperature and heat flux where the Mach number is low and vice versa. Because of the expansion, the momentum as a product of density and velocity decreases: The Reynolds number decrease leads

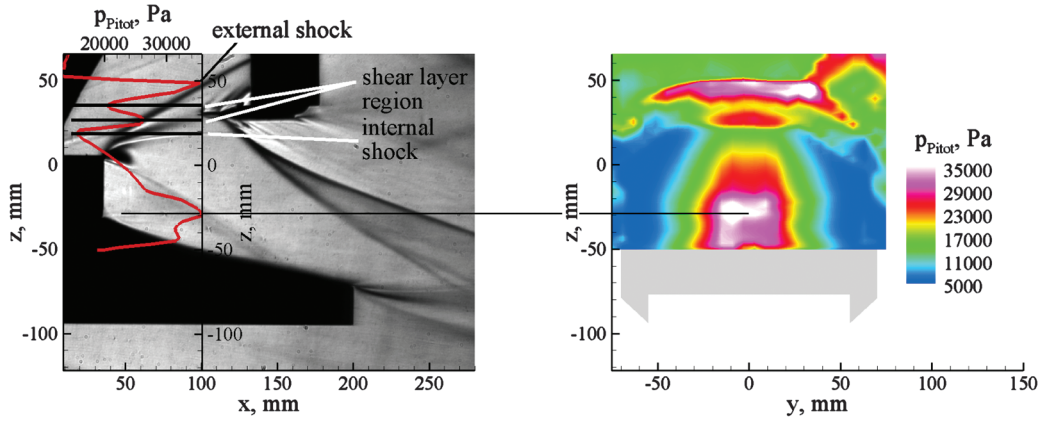

Fig. 19 Comparison of the pitot pressure measurements with a schlieren photograph at $\Pi = 500$ and $x = 150$ mm: left, schlieren photograph and pitot pressure at $y = 0$ mm; right, y–z plane at $x = 150$ mm.

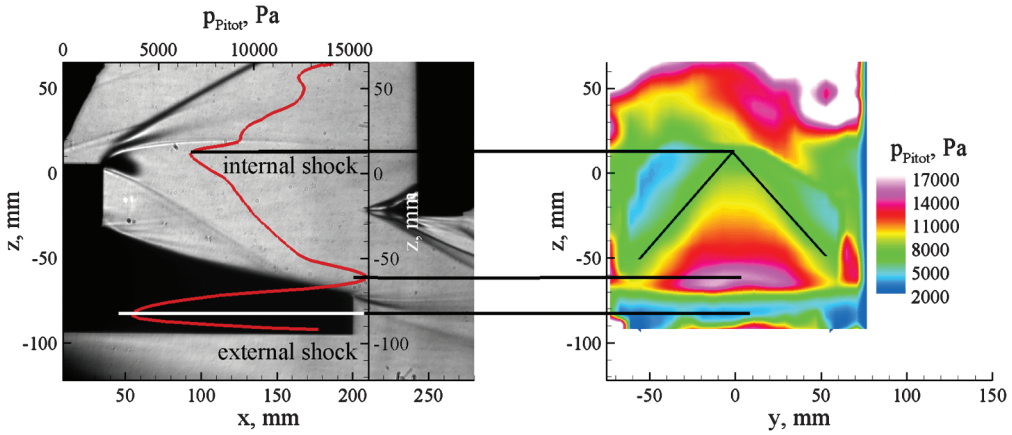

Fig. 20 Comparison of the pitot pressure measurements with a schlieren photograph at $\Pi = 500$ and $x = 210$ mm: left, schlieren photograph and pitot pressure at $y = 0$ mm; right, y–z plane at $x = 210$ mm.

to a thicker boundary layer and lower temperature gradients at the wall. For this reason, the Stanton number decreases in the region where the flow accelerates and increases in the inner region of the nozzle flow where the flow is slower than in the outer region. Compared to the results obtained by the PSP technique [9], it is noticeable that the temperature and pressure distribution quantitatively agree very well. Pressure and temperature have the maximal values in the inner region where the Mach number is the lowest and their minimal values in the outer region where the Mach number is highest.

In Fig. 22, the Stanton number distribution along the y direction at the position $x = 100$ mm is shown at two different nozzle pressure ratios. The values of the Stanton number at the beginning, in the middle, and at the end of the test run are compared. One can state that the Stanton number changes little during the test run and that this deviation is negligible. Comparing the results of the two different nozzle pressure ratios in Figs. 22a and 22b, it is noticeable that the

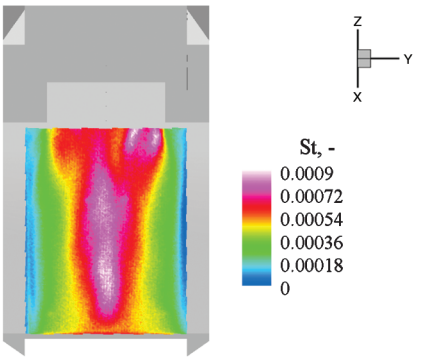

a) Stanton number distribution at Π = 250

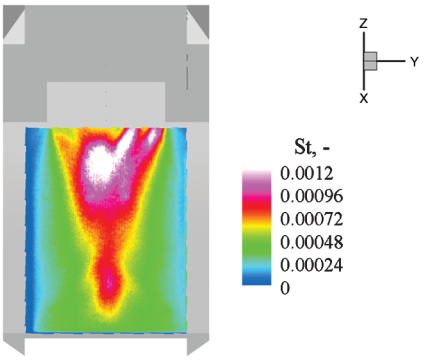

b) Stanton number distribution at Π = 500

Fig. 21 Influence of the nozzle pressure ratio on the Stanton number distribution on the surface of the expansion ramp at $\Pi = 500$ and $Re_U = 8 \times 10^6$.

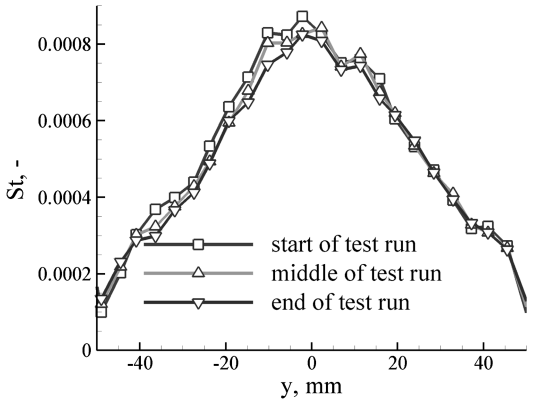

a) Stanton number distribution at Π = 250

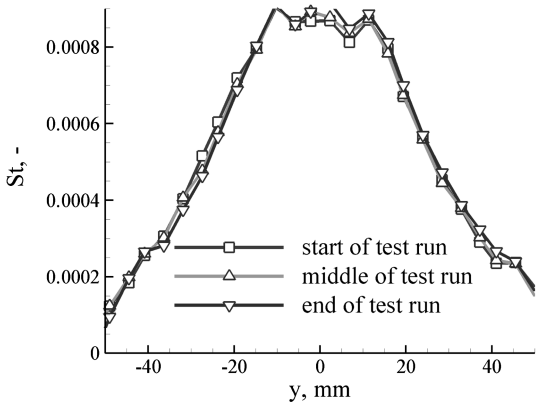

b) Stanton number distribution at Π = 500

Fig. 22 Influence of the nozzle pressure ratio on the Stanton number distribution in y direction at $x = 100$ mm, $Re_U = 8 \times 10^6$, and $T_{0,N} = 580$ K.

maximal values for the Stanton number at $y = 0$ mm is almost identical, $St = 0.0009$. This value, however, is constant over a greater region in the case of $\Pi = 500$ than in the case of $\Pi = 250$. Whereas the higher nozzle pressure ratios leads to a more constant distribution (from $y = -10$ mm to $y = 10$ mm) of the maximal value, the lower nozzle pressure ratio has only a single peak ($y = 0$ mm) with the maximal value. The reason for this is the broader exhaust plume in the y direction at $\Pi = 500$, so that the expansion ramp is covered more uniformly by the flow. In the outer region, the Stanton number decreases to similar values at the two different nozzle pressure ratios. The decline of the Stanton number toward the side of the expansion ramp can be clearly seen in this depiction. In the outer region at $y = 40$ mm and $y = -40$ mm, the

Stanton number declines to $St = 0.0003$. The decline of the Stanton number from the peak value $St = 0.0009$ to $St = 0.0003$ is stronger at $\Pi = 500$. Overall, the area below the curve at $\Pi = 500$ is greater, leading to higher heat loads onto the surface in this case. These measurements provide a map of the regions where the cooling capacity has to be enhanced to avoid material failure.

IV. Conclusions

An experimental study was conducted with a nozzle/afterbody model to characterize the flowfield created by the interaction of a single expansion ramp nozzle flow with an external hypersonic flow. For a better understanding of the physical phenomena with respect to the influence of different parameters on the nozzle flow properties and nozzle performance, as well as to the complex interactions between the internal nozzle and the external flows, the pitot pressure measurement, the schlieren photograph, and the IR thermography methods have been applied.

Pitot pressure measurements provided visualization of the entire flowfield and were most useful in the identification of flow gradients; they could also be used to estimate the size of the exhaust plume and to get the position of shear layers and shocks. From this, information about the flow behavior in the wake of the nozzle and the interaction between the internal and external flow have been extracted. The results show that the nozzle core flow is not influenced by the external flow conditions (i.e., neither by Π, nor Re_U). There is also no influence by the nozzle total temperature. The behavior of the shear layer, however, is greatly influenced by these two parameters. The flowfield with and without external flow has been extensively described and the effects on the base drag discussed. Higher nozzle pressure ratios do not only lead to a higher gross thrust, but also cause a higher base drag.

The results obtained by the pitot pressure measurements have been compared with the schlieren photographs taken during the same test run. This comparison showed a very good agreement concerning the position of shear layers as well as internal and external shocks. The influence of the nozzle total temperature and the nozzle pressure ratio on the exhaust plume was also studied with the schlieren photographs. This method, as well as the pitot pressure measurements, proved the influence of the nozzle total temperature on the exhaust plume to be negligible in the investigated region, whereas the nozzle pressure ratio greatly affects the size of the exhaust plume and the position of shear layer, as well as external and internal shocks. Static pressure measurements also showed that nozzle total temperature does not influence the pressure distribution on the expansion ramp in the investigated region.

The use of IR thermography provided the temperature and Stanton number distribution on the surface of the expansion ramp. These measurements gave insight into the flow topology on the surface of the expansion ramp and supplied information where an effective cooling system is needed in real flight operations. Flow topology and the temperature distribution on the surface of the expansion ramp were not influence by the external flow. The influence of the nozzle pressure ratio on the heat flux and Stanton number distribution, however, has been shown and analyzed. It could be seen that the temperature distribution was very similar to the pressure distribution obtained in earlier experimental studies. Both temperature and pressure distribution are mainly driven by the Mach number distribution that depends on the expansion in x, y, and z directions.

Acknowledgments

The financial support for this work by the German National Research Council within the Graduate Student Research Group "Aerothermodynamic Design of a Scramjet Propulsion System for Future Space Transportation" and by the German Aerospace Center is gratefully acknowledged. The authors would especially like to thank the following colleagues in the Institute of Aerodynamics and Flow technology for their valuable contributions to this work: M. Kosbow, M. Schmors, and D. Lütz.

References

[1] Walther, R., "Scramjet-Propulsion: alte Herausforderung im neuen Jahrhundert?" German Society for Aeronautics and Astronautics, Munich, 2003, pp. 755–764.

[2] Curran, E. T., and Murthy, S. N. B., *Scramjet Propulsion*, Vol. 189, AIAA, Reston, VA, 2000.

[3] Fry, R. S., "A Century of Ramjet Propulsion Technology Evolution," *Journal of Propulsion and Power*, Vol. 20, No. 1, 2004, pp. 27–58. doi:10.2514/1.9178

[4] Spaid, F. W., and Keener, E. R., "Hypersonic Nozzle/Afterbody CFD Code Validation, Part I: Experimental Measurements," AIAA Paper 93-0607, 1993.

[5] Spaid, F. W., Keener, E. R., and Hui, F. C. L., "Experimental Results for a Hypersonic Nozzle/Afterbody Flow Field," NASA TM-4638, 1995.

[6] Gruhn, P., Henckels, A., and Sieberger, G., "Improvement of the SERN Nozzle Performance by Aerodynamic Flap Design," *Aerospace Science and Technology*, Vol. 6, No. 6, 2002, pp. 395–405. doi:10.1016/S1270-9638(02)01177-X

[7] Flandro, G. A., Roach, R. L., and Buschek, H., "Dynamic Interactions Between Hypersonic Vehicle Aerodynamics and Propulsion System Performance," NASA CR-190638, 1992.

[8] Hirschen, C., Gülhan, A., Beck, W. H., and Henne, U., "Experimental Study of a Scramjet Nozzle Flow Using the Pressure Sensitive Paint Method," *Journal of Propulsion and Power*, Vol. 24, No. 4, 2008, pp. 662–672.

[9] Hirschen, C., Gülhan, A., Beck, W. H., and Henne, U., "Measurement of Flow Properties and Thrust on Scramjet Nozzle Using Pressure-Sensitive Paint," *Journal of Propulsion and Power*, Vol. 25, No. 2, 2009, pp. 267–280. doi:10.2514/1.37957

[10] Edwards, T. A., "The Effect of Exhaust Plume/Afterbody Interaction on Installed Scramjet Performance," NASA TM-101033, 1988.

[11] Baysal, O., "Flow Analysis and Design Optimization Methods for Nozzle Afterbody of a Hypersonic Vehicle," NASA CR-4431, 1991.

[12] Ebrahimi, H. B., "An Efficient Two-Dimensional Engineering Design Code for Scramjet Combustor, Nozzle, and Plume Analysis," AIAA Paper 91-0416, 1991.

[13] Ishiguro, T., Takaki, R., Mitani, T., and Hiraiwa, T., "Three-Dimensional Analysis of Scramjet Nozzle Flows," AIAA Paper 1993-5059, 1993.

[14] Tatum, K., Monta, W., Witte, D., and Walters, R., "Analysis of Generic Scramjet External Nozzle Flowfields Employing Simulant Gases," AIAA Paper 90-5242, 1990.

[15] Keener, E. R., "Experimental Research of the Aerodynamics of Nozzles and Plumes at Hypersonic Speeds," NASA CR-187316, 1992.

[16] Carboni, J. D., Shyne, R. J., Leavitt, L. D., Taylor, J. G., and Lamb, M., "Supersonic Investigation of Two Dimensional Hypersonic Exhaust Nozzles," NASA TM-105687, 1992.

[17] Lindblad, I. A. A., Grönland, T. A., Cambier, J.-L., Wallin, S., Behrens, T. M., Sacher, P., and Netterfield, M., "A Study of Hypersonic Afterbody Flowfields," AIAA Paper 97-2289, 1997.

[18] Tomioka, S., Hiraiwa, T., and Mitani, T., "A Study on Boundary Layer in a Scramjet Nozzle Operating under High Enthalpy Conditions," AIAA Paper 1994-2820, 1994.

[19] Weigand, B., Gaisbauer, U., Reinhartz, B., Kau, H.-P., and Schröder, W., "Aero-thermodynamische Auslegung eines Scramjet-Antriebssystems für zukünftige Raumtransportsysteme," German Society for Aeronautics and Astronautics, Munich, 2006.

[20] Mitani, T., Kanda, T., Hiraiwa, T., Igarashi, Y., and Nakahashi, K., "Drags in Scramjet Engine Testing: Experimental and Computational Fluid Dynamics Studies," *Journal of Propulsion and Power*, Vol. 15, No. 4, 1999, pp. 578–583. doi:10.2514/2.5466

[21] Hirschen, C., Gruhn, P., and Gülhan, A., "Influence of Heat Capacity Ratio on the Interaction Between External Flow and Nozzle Flow of a Scramjet," AIAA Paper 2006-8095, 2006.

[22] Hirschen, C., Gülhan, A., Beck, W. H., and Henne, U., "Experimental Study of the Interaction between Internal and External Flows of a Scramjet Nozzle using Various Diagnostic Techniques," AIAA Paper 2007-5088, 2007.

[23] Gaisbauer, U., Weigand, B., Reinartz, B., Kau, H. P., and Schröder, W., "Research Training Group GRK 1095/1: Aero-Thermodynamic Design of a Scramjet Propulsion System," AIAA, Reston, VA, 2007.

[24] Hirschen, C., and Gülhan, A., "Experimental Study of the Single Expansion Ramp Nozzle Flow Properties and its Interaction with the External Flow," Deutsche Gesellschaft fr Luft- und Raumfarht Paper 367, 2007.

[25] Gülhan, A., "Application of Pyrometry and IR-Thermography to High Surface Temperature Measurements," NATO Research and Technology Organisation, RTO EN-8, 1999.
[26] Henckels, A., and Gruhn, P., "Study on Aerothermal Effects of Viscous Shock Interaction in Hypersonic Inlets," ESA SP-253, 2004.
[27] Häberle, J., and Gülhan, A., "Internal Flowfield Investigation of a Hypersonic Inlet at Mach 6 with Bleed," *Journal of Propulsion and Power*, Vol. 23, No. 5, 2007, pp. 1007–1017. doi:10.2514/1.29669
[28] Tatum, K. E., and Huebner, L. D., "Exhaust Gas Modeling Effects on Hypersonic Powered Simulation at Mach 10," AIAA Paper 1995-6068, 1995.
[29] Hiraiwa, T., Tomioka, S., Ueda, S., and Mitani, T., "Performance Variation of Scramjet Nozzle at Various Nozzle Pressure Ratios," *Journal of Propulsion and Power*, Vol. 11, No. 3, 1995, pp. 403–408. doi:10.2514/3.23858
[30] Gruhn, P., "Einfluss einer Heckklappe auf die Düsenströmung im Hyperschall," Aachen Univ. of Technology, Aachen, Germany, 2004.

R. Bowersox
Associate Editor